The Influences of TOVS Radiance Assimilation on Temperature and Moisture Tendencies in JRA-25 and ERA-40

MASAMI SAKAMOTO

Numerical Prediction Division, Japan Meteorological Agency, Tokyo, Japan

JOHN R. CHRISTY

Earth System Science Center, University of Alabama in Huntsville, Huntsville, Alabama

ABSTRACT

A Japanese long-term reanalysis (JRA-25) was completed in 2006 utilizing the comprehensive set of observations from the 40-yr ECMWF Re-Analysis (ERA-40). JRA-25 and ERA-40 adopted the same type of assimilation systems: 3DVAR with direct use of satellite sounding radiances. Long-term upper-air thermal tendencies in both reanalyses are examined and compared with the observational deep-layer temperatures of the University of Alabama in Huntsville (UAH) and Remote Sensing Systems (RSS). The upper-air temperature tendencies in the reanalyses are significantly different from those of UAH and RSS, and they appear to be influenced by the way the observations of the Television and Infrared Observation Satellite (TIROS) Operational Vertical Sounder (TOVS) are used.

This study focuses on documenting problems in TOVS assimilation, especially problems in bias corrections used in the reanalyses. Referring to quantitative results in an examination of biases between the reanalyses and raw TOVS observations, this study identifies (i) spurious thermal tendencies derived from transitions in TOVS and in the reanalysis calculation streams, (ii) an excessive enhancement of the tropical water cycle in ERA-40, and (iii) an excessive cooling trend and unstable behavior in the stratospheric temperature in JRA-25.

The results of this study suggest that any inconsistencies in TOVS usage can lead to serious inconsistencies in the reanalyses. Therefore, time-consuming efforts to obtain reliable observational information from TOVS are necessary for further progress in reanalyses.

1. Introduction

The European Centre for Medium-Range Weather Forecasts (ECMWF) produced a 40-yr Re-Analysis known as ERA-40 in 2003 (Uppala et al. 2005). ERA-40 was based on improvements to two pioneering reanalyses: the National Centers for Environmental Prediction–National Center for Atmospheric Research (NCEP–NCAR) reanalysis (Kalnay et al. 1996) and ERA-15 (Gibson et al. 1997). Given the length of the target period (September 1957–August 2002), ERA-40 has been a focus of climate variation studies (e.g., Santer et al. 2004; Christy et al. 2006). Such reanalyses are potentially valuable to help address one of the most important issues today—the response of the climate system to human-induced changes such as the enhancement of the natural greenhouse effect. Trend precision of global upper-air temperature on the order of ± 0.05 K decade^{-1} or less is required to help explain how the temperature responds to changing forcing. To date, the precision for temperature changes over the decadal time frame in long-term reanalyses has been found to be subject to uncertainties greater than this goal (Karl et al. 2006).

The Japan Meteorological Agency (JMA) and the Central Research Institute of Electric Power Industry (CRIEPI) completed a 26-yr (January 1979–December 2004) reanalysis known as JRA-25 (Onogi et al. 2007, 2005). JRA-25 utilized the comprehensive observational dataset developed for ERA-40, and both reanalyses used the same type of assimilation systems: three-dimensional variational data assimilation (3DVAR) with direct assimilation of observed radiances from the Television and Infrared Observation Satellite (TIROS)

Corresponding author address: Masami Sakamoto, Numerical Prediction Division, Japan Meteorological Agency, 1-3-4, Otemachi, Chiyoda, Tokyo 100-8122, Japan.
E-mail: masami.sakamoto-a@met.kishou.go.jp

Operational Vertical Sounder (TOVS; Smith et al. 1979; Werbowetzki 1981) on board the National Oceanic and Atmospheric Administration (NOAA) satellites.

We begin this study with brief descriptions of the observational datasets followed by comments on the systems employed in generating the reanalyses. We also describe the microwave-based deep-layer temperature products. Then JRA-25 and ERA-40 will be compared with the observational temperature products. From these results, we will discuss the issues related to the TOVS assimilation. The purpose of this paper is to report problems in the TOVS assimilation in the reanalyses and how these impact the upper-air temperature and moisture tendencies. These results will contribute to better application practices of TOVS in future reanalyses.

2. The reanalyses and the deep-layer temperature products

In this section, we briefly describe JRA-25 and ERA-40, focusing on their differences. We then provide a review of the microwave-based observational products. This will provide readers with a basic knowledge of the datasets. [Details are found in Onogi et al. (2007), Uppala et al. (2005), Christy et al. (2003), and Mears et al. (2003).]

a. Observations and forecast/data assimilation systems in JRA-25 and ERA-40

1) OBSERVATIONS

JRA-25 was constructed using the operational numerical weather prediction (NWP) techniques of JMA and computational resources in CRIEPI. However, neither organization possessed a comprehensive observation dataset to apply to a global long-term reanalysis. ECMWF provided JMA with the ERA-40 observing system. ECMWF collected various datasets from organizations worldwide for use in the assimilation activity (Uppala et al. 2005). This is comprehensive and includes level-1c data of the TOVS and advanced TOVS (ATOVS) observations, where the level-1c data are the calibrated data of brightness temperature (BT). Therefore the TOVS observations used in JRA-25 were identical to those in ERA-40.

Although there were some observations originally prepared for JRA-25 (Onogi et al. 2007, 2005), like the tropical cyclone wind by Fiorino (2002) and the reprocessed wind from the Geostationary Meteorological Satellite (GMS; Oyama 2007), JRA-25 observational data were very similar to those of ERA-40 until around March 2001 when JMA's data storage system was updated.

Important for upper-air temperature values are radiosonde observations (raob). JRA-25 bias adjustment for raob was similar to that of ERA-40 (Andræ et al.

2004), in which major gaps in time series for each site were filled.

2) FORECAST AND DA SYSTEMS

Table 1 summarizes the forecast and data assimilation (DA) systems for JRA-25 and ERA-40. Both systems are not necessarily as conservative in energy, mass, and flow as systems used in global warming experiments. Neither reanalyses included atmosphere–ocean coupled forecasting systems nor the effect of realistic variations of CO_2 and other radiatively active atmospheric constituents, except for ozone data in JRA-25, because both reanalyses intended to depict realistic climatic features using DA.

With modifications, JRA-25 utilized the JMA Global Spectral Model (GSM) version 0103 (JMA 2002) and used the following datasets to constrain atmospheric behavior: Centennial In-Situ Observation-Based Estimates of Variability of SST and Marine Meteorological Variables (COBE; Ishii et al. 2005) and ozone concentrations prepared by JMA. COBE SST/sea ice data were used as oceanic boundary conditions. The ozone data were prepared by the Atmospheric Environmental Division (AED) of JMA using the National Aeronautics and Space Administration's (NASA) Total Ozone Mapping Spectrometer (TOMS) observations and a chemical-transport model in JMA. The ozone data were introduced into GSM to estimate the absorption of radiation. GSM0103 had a cold bias in the lower- and midstratosphere, which came from an estimation error of longwave radiational absorption (Murai et al. 2005).

Descriptions of ERA-40's forecast and DA systems are found in Uppala et al. (2005), Jakob et al. (2000), and Simmons et al. (1999), and the system is based on Integrated Forecast System (IFS) cycle 21r4 (Jakob et al. 2000). The semi-Lagrangian advection scheme (SL) was introduced at cycle l8r5 (the system introduced in April 1998). Horizontal resolution of a T159 SL forecast model is finer than that of a T106 Euler model (Uppala et al. 2005). The radiational parameterization in ERA-40 used ozone distribution data in IFS, but ozone concentration became one of the prognostic variables at cycle 21r4 (Dethof and Hólm 2004). As for oceanic boundaries, ERA-40 used NOAA/NCEP SST (Reynolds et al. 2002). Since ERA-40 selected 3DVAR (the default in cycle 21r4 was 4DVAR), a scheme named FGAT (the first guess at an appropriate time) was used in which observational innovations are calculated and compared with the first guess at the nearest forecast time. ERA-40 adopted larger forecast errors for all the observations including TOVS than is done in ECMWF's NWP operation to make use of the original observation tendencies more clearly.

TABLE 1. Features of forecast and assimilation systems of JRA-25 and ERA-40. The features of ERA-40 are after Uppala et al. (2005).

	Forecasting system	
	JRA-25	ERA-40
Model version	Modified JMA operational spectral model: GSM0103 (Euler spectral model)	IFS cycle CY21r4 with modifications (semi-Lagrangian spectral model)
Resolution	T106 L40	T159 L60
SST/sea ice	JMA's COBE dataset (Ishii et al. 2005)	Weekly NOAA/NCEP 2DVAR dataset (Reynolds et al. 2002)
Ozone dataset	Radiational parameterization input: JMA/AED ozone	Radiational parameterization: Ozone distribution data in IFS
	No chemical transport process in the forecast model	Chemical transport output: A prognostic variable of IFS (Dethof and Hólm 2004)
	Data assimilation system	
	JRA-25	ERA-40
System version	JMA operational 3DVAR: Takeuchi and Tsuyuki (2002)	3DVAR of CY21r4: Jakob et al. (2000)
Modified features	Assimilation of TOVS and SSM/I total column water vapor	FGAT

To ensure consistency for climate purposes, the entire period of a reanalysis should be governed by a single calculation stream because the first guess forecast and bias correction for each observation should be consistent throughout. However, both reanalyses divided the whole target periods into several calculation streams because of practical considerations. Figure 1 shows the calculation streams of the reanalyses after 1979 when TOVS observations are utilized.

3) TOVS QUALITY CONTROL SYSTEMS

Because JMA had never employed an operational direct assimilation of TOVS BT, JRA-25 developed a TOVS quality control procedure, which is summarized in the appendix. As for ATOVS, JRA-25 adopted the JMA operational ATOVS system, which came into operation in March 2005. The ATOVS system used observations from the Advanced Microwave Sounding Unit (AMSU) but did not use the infrared sounder. The TOVS and ATOVS systems in JRA-25 used different versions of the radiative transfer models; the TOVS system used the fast radiative transfer model (RTTOV) version 6 (Saunders et al. 1999) and the ATOVS system used RTTOV version 7. Therefore, both systems could not be used simultaneously. JRA-25 switched the satellite sounding system from TOVS to ATOVS at the
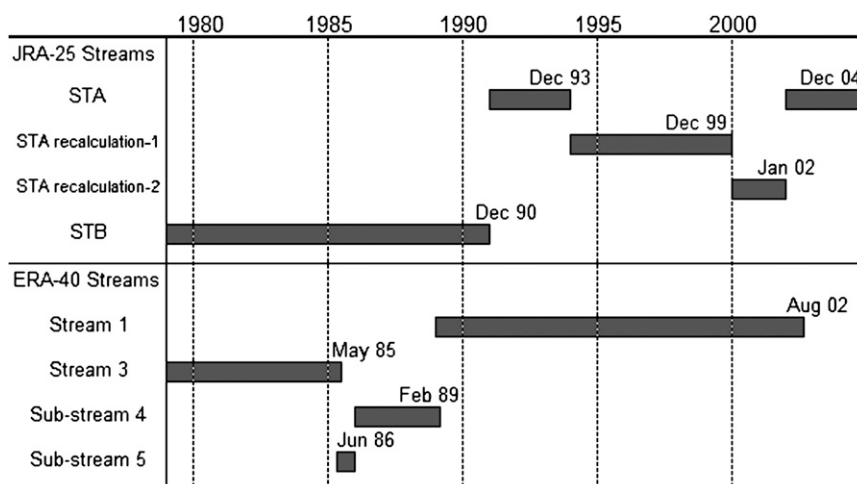

FIG. 1. Calculation streams of JRA-25 and ERA-40. The months shown are the months when the calculation streams finished. Note the calculation stream A (STA) of JRA-25 started in 1989, but was replaced by the calculation stream B (STB) (until December 1990), STA recalculation 1 (January 1994–December 1999), and STA recalculation 2 (January 2000–January 2002).

beginning of November 1998. The JRA-25 TOVS system adopted an adaptive bias correction scheme (see appendix), while the ATOVS system used fixed coefficients derived from the JMA NWP operation.

In ERA-40, the TOVS/ATOVS bias correction scheme is based on the technique of Harris and Kelly (2001). Although they introduced an adaptive adjustment procedure in the ECMWF NWP operation, ERA-40 bias correction coefficients were fixed after being examined in short-term passive uses in advance of the actual uses.

b. The observational deep-layer temperature products

Following different paths for generating atmospheric temperatures, the University of Alabama in Huntsville (UAH) and Remote Sensing Systems (RSS) have focused on the time series of the bulk atmospheric temperatures from the Microwave Sounding Unit (MSU) and AMSU. The original effort for such temperature products dates back to the early 1990s (Spencer and Christy 1990), and the original layer-definitions are found in Spencer and Christy (1992a,b). Since then, problems have been found in the raw data and processing choices, and those discovered have been adjusted to construct consistent sequences of upper air temperature datasets.

To generate time series of microwave BT from the sensors' digital counts, the UAH and RSS independently compute BT through a quadratic equation that relates the earth-view counts to BT based on two calibration points: the cold-space counts in the cold-space view ($\sim$2.7 K) versus the onboard hot-target counts with a monitored hot-target temperature. The obtained BT was adjusted for spacecraft drifts through the diurnal cycle and instrumental response characteristics to varying solar influence on the instrument itself. These time series of BT are finally adjusted by empirically determined bias corrections and drift adjustments to remove the differences observed by two simultaneously operating spacecraft. These drifts and biases usually develop during the rigors of launch into the environment of space and/or through orbit decays and orbital drifts during long operational periods. These can introduce spurious climate trends (Christy et al. 2000).

These products are extended to the ATOVS observation era, and three types of products have been used to investigate vertical thermal structures and long-term tendencies. These products monitor temperature in the lower troposphere (TLT; sensitive to emissions from the surface to $\sim$350 hPa), temperature in the midtroposphere (TMT; from surface to $\sim$75 hPa), and temperature in the lower stratosphere (TLS; from about 130 to $\sim$20 hPa). Further information about these three are found in Christy et al.

(2003). For this study, we use UAH version 5.2 and RSS version 3.1 for TLT, and UAH version 5.1 and RSS version 3.2 for TMT and TLS (Mears et al. 2003).

3. Comparison of atmospheric temperature tendencies

We compare, in this section, JRA-25 and ERA-40 with UAH and RSS to clarify the differences among them. Since UAH and RSS are derived from the TOVS and ATOVS observations, results will show how the reanalyses differ from the observations because of assimilation procedures and other factors. We shall describe how we shall calculate TLT, TMT, and TLS from the reanalyses in this section. Then we compare these from the reanalyses with UAH and RSS. We shall also present comparisons for the High Resolution Infrared Radiation Sounder (HIRS) and the stratospheric sounding unit (SSU). Such a general survey in the TOVS BT field will provide us with clues to investigate where the differences came from and what the underlying problems are.

a. How to estimate BTs and the deep-layer temperatures from the reanalyses

Monthly averaged reanalysis data at 2.5° grid points are translated into BT. We execute the forward calculation of RTTOV version 6 (Saunders et al. 1999) to estimate BT from the reanalyses. Since both JRA-25 and ERA-40 used RTTOV version 6 to determine the first guess and increment for TOVS BT, RTTOV will provide analyzed values in TOVS BT for both reanalyses. We prepare TLT, TMT, and TLS using the retrieval procedure documented in Christy et al. (2003, 2000), which requires the linear combinations of BTs in different scan positions from MSU channel 2 (needed for TLT and TMT) and channel 4 (for TLS). We calculate monthly normals for the period from January 1979 to December 2001, and convert each monthly value to an anomaly. We also prepare anomalies of UAH and RSS products using normals for the same period.

In section 3c, we calculate monthly averaged BT for each channel of three instruments using monthly average gridpoint data again. The calculation is done only for subsatellite points without variations in surface properties and cloudiness factored in. Therefore there are no corresponding BT observations for HIRS and SSU, which do not have scan positions at nadir. We compare anomalies of BTs using the normal from January 1979 to December 2001.

b. Comparisons of TLT, TMT, and TLS

Anomaly time series of global TLT of JRA-25, ERA-40, UAH, and RSS and the differences are displayed in
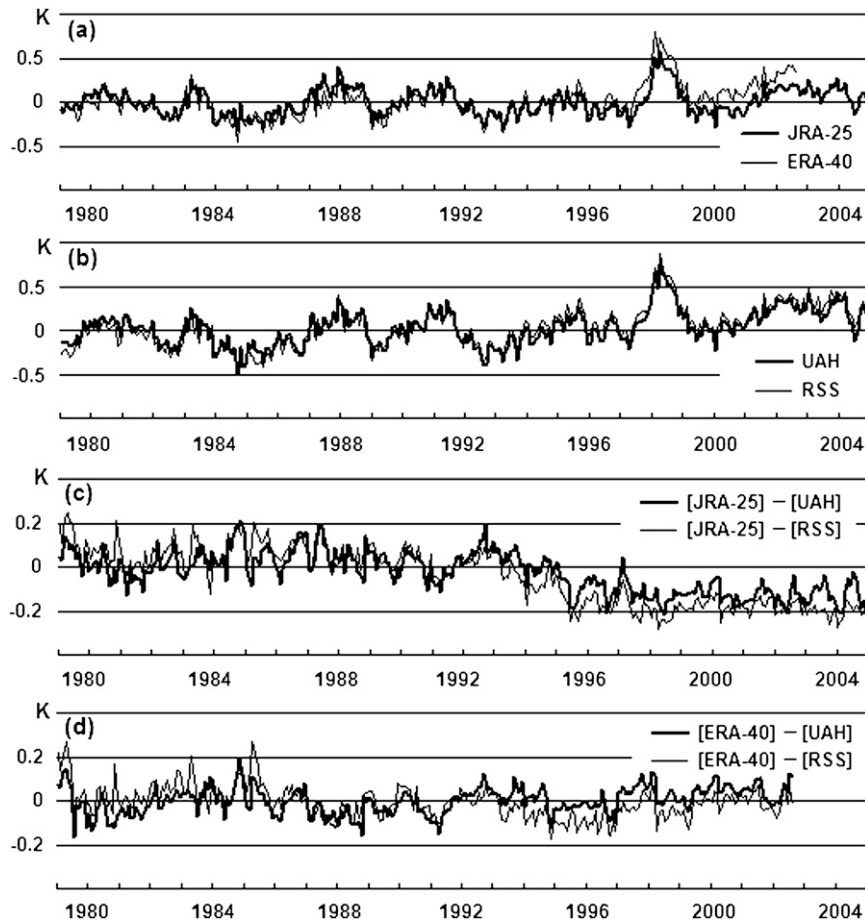
FIG. 2. Monthly anomaly time sequences of global average TLT (K) of (a) JRA-25 and ERA-40 and (b) UAH version 5.1 and RSS version 3.1. Differences of (c) JRA-25 and (d) ERA-40 from UAH and RSS. The normal is calculated for the period 1979–2001.

Fig. 2. The global TLT anomaly of JRA-25 is noticeably cooler than others since the later half of the 1990s (Figs. 2a,c). The JRA-25 switch from TOVS to ATOVS in November 1998 seems to be one reason for this. The forecast model response to the El Niño–Southern Oscillation (ENSO) event from 1997 to 1998 might be another potential reason. The tropical (20°S–20°N) average TLTs are displayed in Fig. 3. Figure 3a shows slightly different tendencies between the reanayses for each El Niño event (1982–83, 1986–88, 1991–92, and 1997–98). RSS seems to be warmer than others since 1993 (Figs. 2b–d). *NOAA-11* and *-12* were in operation in 1993. Christy and Norris (2006) intercompared UAH and RSS TLT with one family of raob (viz., at 31 stations) and discovered differences in the adjustments necessary for the inclusion of *NOAA-12* and in the calibration and diurnal drifting of *NOAA-11* with RSS showing a shift to relatively warmer temperatures (Christy et al. 2007; Randall and Herman 2008). Trends for 1979–2001 are given in Table 2 where UAH and ERA-40 indicate

similar TLT trends ($+0.091$ and $+0.115$ K decade^{-1}), while RSS is more positive ($+0.163$) and JRA-25 less positive ($+0.012$).

Geographical distributions of anomaly TLT trends for the reanalyses are shown in Fig. 4. The negative trend of JRA-25 in the high southern latitudes is apparent and such cooling trends are commonly seen among the MSU-derived observational datasets (Mears and Wentz 2005). This difference might be related to the difference in SST and sea ice datasets. JRA-25 used the COBE dataset, which shows quite similar tendencies to NOAA/ NCEP SST over the tropics and subtropics but slightly different tendencies in the polar regions (Ishii et al. 2005). Positive trends extending from the subtropics to the midlatitudes over ocean are apparent in ERA-40. The satellite-derived datasets also show disagreements in these areas (see Fig. 13 of Mears et al. 2003). JRA-25 shows a large negative trend in the Amazon basin while ERA-40 shows negative trends over the interior of the African continent. A decreasing trend of JRA-25
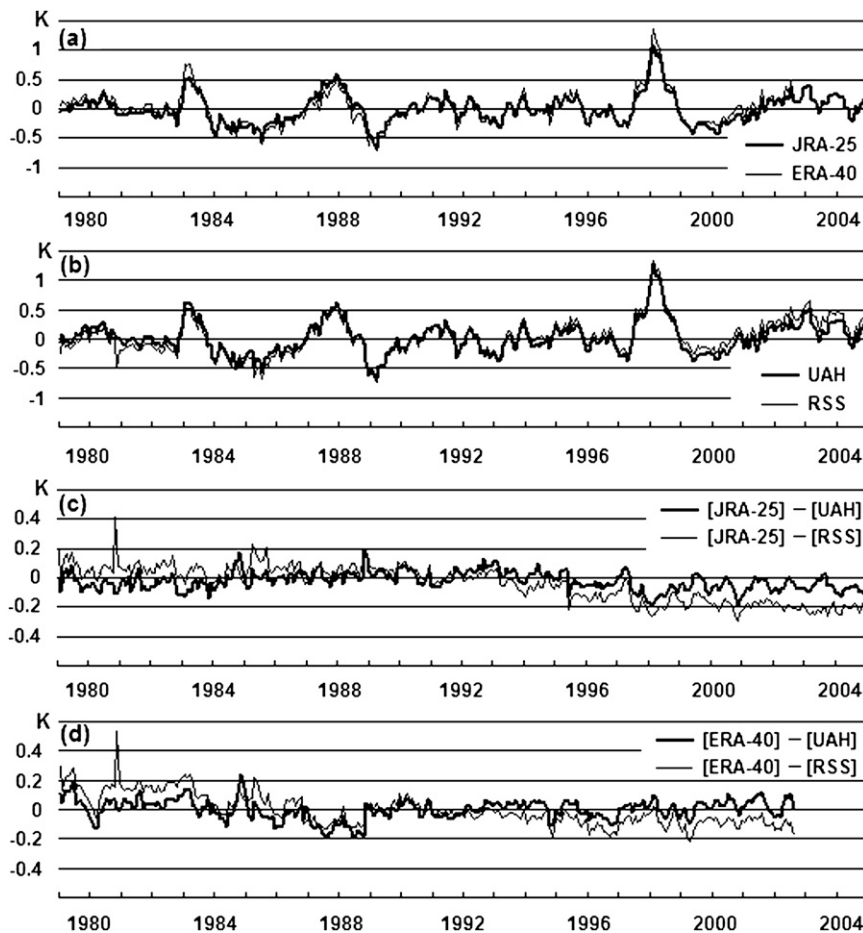
FIG. 3. Monthly anomaly time sequences of TLT (K) averaged over the tropics (20°S–20°N) and their differences. The layout is the same as in Fig. 2.

precipitation over the Amazon area seems closely related to JRA-25 negative thermal trend around the region (Onogi et al. 2007, 2005).

Anomaly time series of global TMT are displayed in Fig. 5. JRA-25 is the warmest during 1986–88 and the coolest during 1997–2002, producing a negative trend, while ERA-40 shows several sudden jumps by ~0.1 K in Fig. 5d. TMT includes a significantly cooling stratospheric contribution related to the negative ozone trends. Therefore the trends in TMT should be less positive than in TLT. Relative to their own TLT trends, UAH and RSS TMT trends are cooler by ~0.08 K decade^{-1} while JRA-25 and ERA-40 are cooler by only ~0.02 K decade^{-1}. Fu et al. (2004) and Christy and Norris (2006) showed that, for a specific region and a specific time period, there are fixed relationships among the bulk layer temperatures. Using adjusted raob datasets, like the Hadley Centre Atmospheric Temperatures version 2 (HadAT2; Thorne et al. 2005) and the Radiosonde Atmospheric Temperature Products for Assessing Cli-

mate (RATPAC; Free et al. 2005), the relative difference in trends between TLT and TMT for the period 1979–2004 is estimated to be ~0.10 K decade^{-1} (Lanzante et al. 2006). Although the periods are different here, the magnitude of the difference is much closer to those of UAH and RSS than ERA-40 and JRA-25. The TLT trends of the reanalyses seem to be not positive enough and/or the TMT trends seem to be too positive. We suspect JRA-25 TLT to be not positive enough, while ERA-40 TMT is too positive (see later).

TABLE 2. Linear trends and estimation errors for each parameter (K decade^{-1}) for the period from 1979 to 2001. Estimations are based on the least squares method. Error ranges are calculated with 95% confidence.

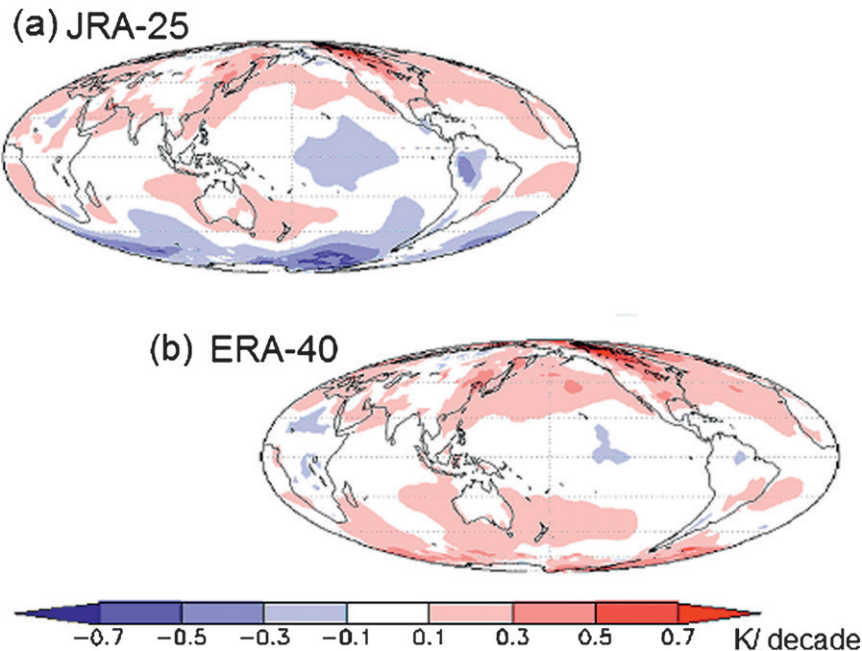| Dataset name	TLT	TMT	TLS
JRA-25	0.012 ± 0.014	−0.011 ± 0.016	−0.418 ± 0.044
ERA-40	0.115 ± 0.016	0.088 ± 0.015	−0.291 ± 0.033
UAH	0.091 ± 0.017	0.014 ± 0.016	−0.520 ± 0.033
RSS	0.163 ± 0.017	0.074 ± 0.016	−0.410 ± 0.033

(a) JRA-25

(b) ERA-40

FIG. 4. Horizontal distribution of TLT anomaly trends (K decade^{-1}) of (a) JRA-25 and (b) ERA-40 for the period from 1979 to 2001.

Figure 6 shows the global anomaly time series of TLS for each dataset and the differences. JRA-25 TLS has large unstable differences relative to the others (Figs. 6a,c) until around November 1998 when JRA-25 switched from the TOVS system to the ATOVS system. We suspect the adaptive bias adjustment for TOVS BT in JRA-25 is a major cause. The most apparent jump is in 1995, when the global anomaly of JRA-25 TLS dropped by about 0.5 K at the beginning of 1995, then jumped up by more than 1.5 K in March (Fig. 6a). *NOAA-11*'s first observation period expired at the end of 1994 and *NOAA-12* did not have an SSU. Thus there was no reliable observational platform in the upper- and midstratosphere until the advent of *NOAA-14* in late February 1995. TLS has considerable contribution from the middle stratosphere, and the GSM used in JRA-25 has a cool bias in the middle and lower stratosphere as noted in section 2a. ERA-40's anomaly TLS seems to be close to that of UAH and RSS, but Fig. 6d shows several jumps by ~0.2 K in its global TLS.

c. Comparison of estimated BTs for all instruments of TOVS

Figure 7 shows the global anomalies of estimated BTs of both reanalyses and their difference. The peak of the weighting function and the absorbing gases of each channel are shown in Table 3.

ERA-40 shows larger anomalies in SSU channels 2 and 3, which are sensitive to the upper-stratospheric temperature, while larger anomalies for JRA-25 are seen in HIRS channels 2 and 3 and MSU channel 4, which are sensitive to the lower-stratospheric temperature (Figs. 7a,b).

JRA-25 also shows a recognizable anomaly in HIRS channel 9, which is sensitive to the radiative absorption and emission by ozone. ERA-40 shows a small anomaly for this channel, and the anomaly of this channel in ERA-40 resembles that of the infrared window channel (HIRS channel 8).

ERA-40 has noticeable anomalies in HIRS channels 11 and 12 (Fig. 7b), which are sensitive to water vapor's radiance emission in the lower and upper troposphere, respectively. ERA-40's simulated HIRS channel 12 shows a significant positive trend from the 1980s to 1990s (Fig. 7b). These are very different from JRA-25 (Fig. 7c).

The differences in the tendencies of estimated BT anomalies from the reanalyses found in this subsection are discussed in the next section showing some important relationships with large-scale climatic features in the reanalyses.

4. Comparison with the raw radiance and discussion

In this section, we shall link some problems in climatic features in both reanalyses to the problems in radiance fields we have shown above. We will compare observed and simulated BTs to quantitatively discuss the usage of TOVS BT as potential factors to account for such problems.
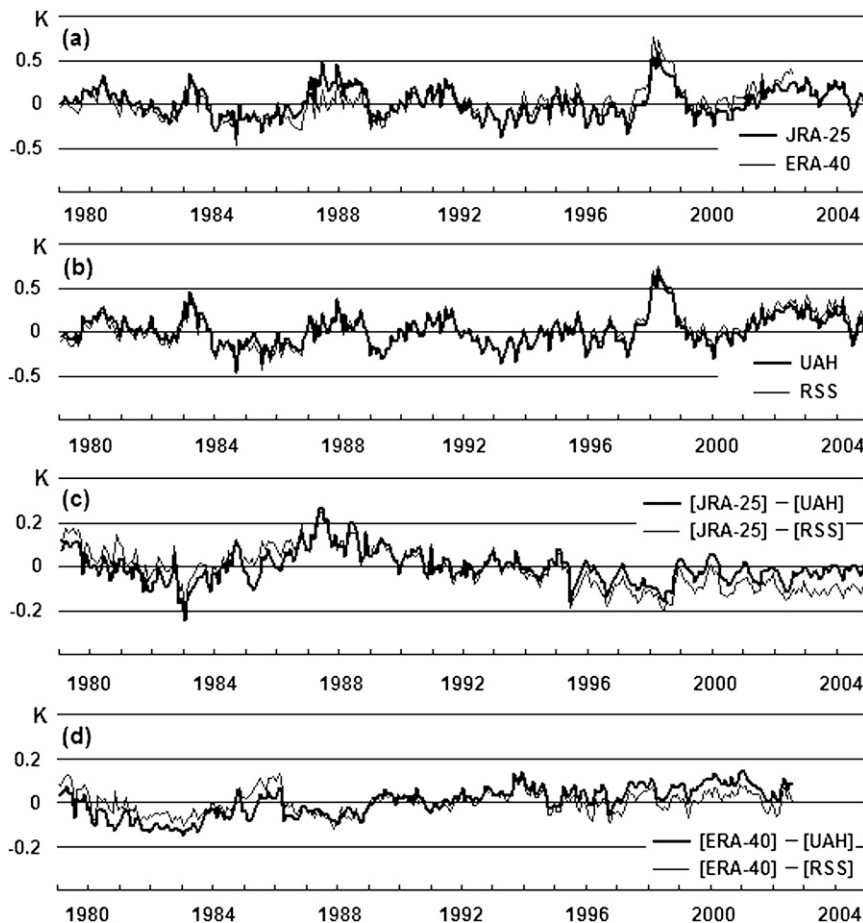
FIG. 5. Monthly global anomaly time sequences of TMT (K) and their differences. The layout is the same as in Fig. 2.

a. How to assess the reanalyses from the radiance field

We will discuss the biases between TOVS observations and the reanalyses, considerable portions of which may come from the bias correction procedure used in the reanalyses. To match the reanalyses and the radiances, atmospheric profiles and surface variables of the reanalyses from the closest analysis time are interpolated to the location of each satellite observation to construct simulated BT (hereafter BT*, meaning reanalyses BT) corresponding to each TOVS observation using the RTTOV version 6 forward model. As mentioned in section 2a, both reanalyses used the same TOVS observations. We use JRA-25 coupled BT data mentioned in the appendix. The vertical interpolation method used here is the log-p linear interpolation, and horizontally the 2.5° grid reanalyses data are bilinearly interpolated to the observation's position. Limb scans will not be used, because they have wide instantaneous fields of view (IFOV), and they seem to be difficult to

simulate accurately when we use RTTOV version 6, in which the single line path approximation is applied. As for channels that are sensitive to the troposphere, only clear sky observations over the ocean are used as were applied to JRA-25 (see appendix). Such procedures are important for accurate comparisons, because cloud contamination has a serious impact on IR channels but detailed cloud information necessary to generate an accurate radiance simulation is not available in either reanalysis. Some microwave channels are sensitive to surface emissivities, however land surface emissivities are not available either.

The following two metrics are defined to diagnose the usage of TOVS observations with the aid of the assimilation theory of 3DVAR. First is departure in BT (DB). We calculate a monthly average of the difference (BT − BT*) along the satellite track and name it DB. We use DB (and its vector for all channels available: $\mathbf{D}_b$) to discuss the bias correction used in the reanalyses:

$$\mathbf{D}_b \equiv \mathrm{gavg}(\mathbf{y}_o - \mathbf{Hx}_a) = \mathrm{gavg}(\mathbf{y}_o - \mathbf{y}_a), \qquad (1)$$
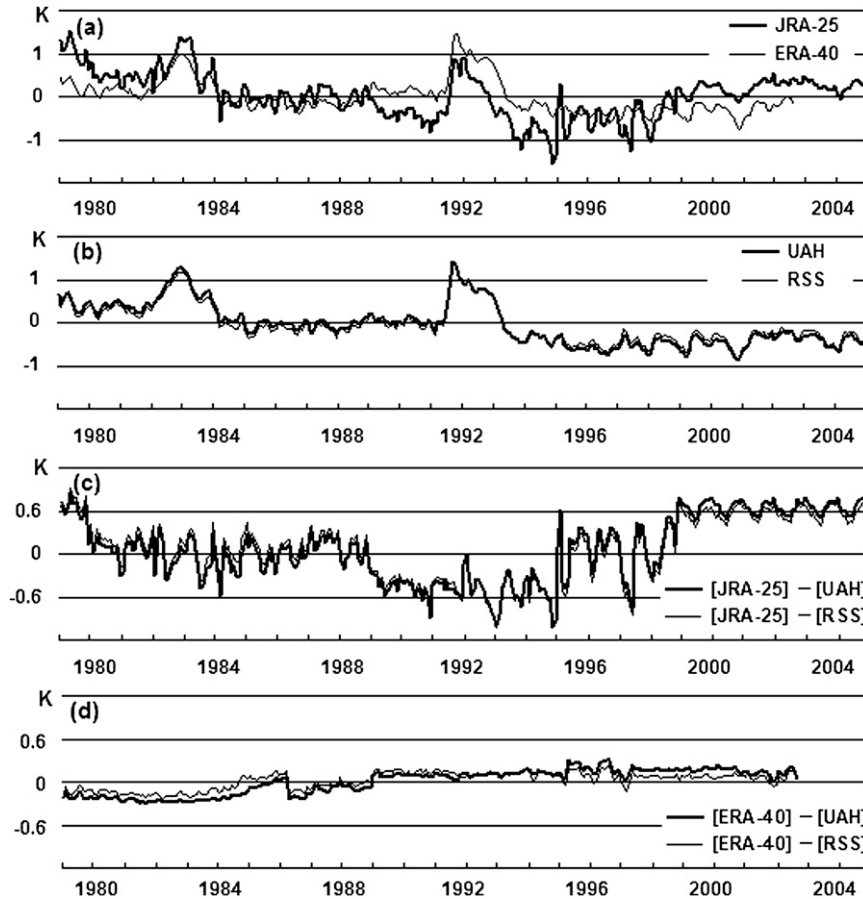
FIG. 6. Monthly global anomaly time sequences of TLS (K) and their differences. The layout is the same as in Fig. 2.

where $\mathbf{y}_o$ is an observation vector of BT, $\mathbf{H}$ is the observation forward operator including temporal and spatial interpolations, $\mathbf{x}_a$ is an analysis gridpoint value vector (reanalysis), $\mathbf{y}_a$ is a vector of BT*, and gavg() means a temporal average of globally distributed data. The increment in assimilation, which means the analysis minus first guess (forecast), is shown as a product of the Kalman gain and a departure from the first guess (observation minus forecast); that is,

$$\mathbf{x}_a - \mathbf{x}_b = \mathbf{K}(\mathbf{y}_o - \mathbf{y}_b) = \mathbf{B}\mathbf{H}^T(\mathbf{R} + \mathbf{H}\mathbf{B}\mathbf{H}^T)^{-1}(\mathbf{y}_o - \mathbf{H}\mathbf{x}_b),$$
(2)

where $\mathbf{x}_b$ is the first guess, $\mathbf{K}$ is the Kalman gain, and $\mathbf{y}_b$ is an estimated BT vector from the first guess ($\mathbf{y}_b = \mathbf{H}\mathbf{x}_b$). In 3DVAR, $\mathbf{K} = \mathbf{B}\mathbf{H}^T(\mathbf{R} + \mathbf{H}\mathbf{B}\mathbf{H}^T)^{-1}$, where $\mathbf{B}$ is the forecast error covariance matrix for the forecast model and $\mathbf{R}$ is the covariance matrix of the observation error; $\mathbf{B}$ and $\mathbf{R}$ are previously known in 3DVAR. We assume that neither $\mathbf{B}$ or $\mathbf{R}$ were locally optimized in the reanalyses. Then, we obtain from Eqs. (1) and (2)

$$\mathbf{D}_b = \text{gavg}[\mathbf{I}(\mathbf{y}_o - \mathbf{y}_b) - \mathbf{H}(\mathbf{x}_a - \mathbf{x}_b)]$$

$$\cong \mathbf{R}(\mathbf{R} + \mathbf{H}\mathbf{B}\mathbf{H}^T)^{-1}\text{gavg}(\mathbf{y}_o - \mathbf{y}_b),$$
(3)

where $\mathbf{I}$ is the unit matrix. The assimilation theory of 3DVAR requires that there is no bias between gavg($\mathbf{y}_o$) and gavg($\mathbf{y}_b$). However, in reality observations and estimated values do have biases. To obtain a reasonable assimilation result, assimilation scientists use a bias correction ($\mathbf{b}_c$) so that
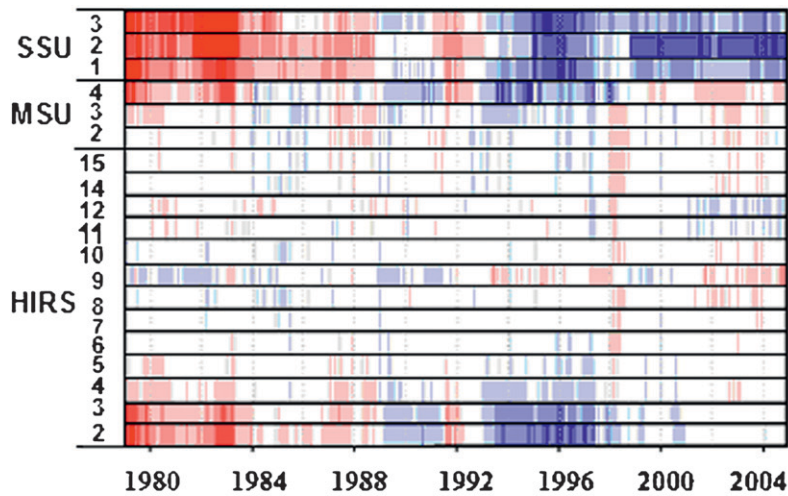
$$\text{gavg}(\mathbf{y}_o - \mathbf{b}_c) \cong \text{gavg}(\mathbf{y}_b).$$
(4)

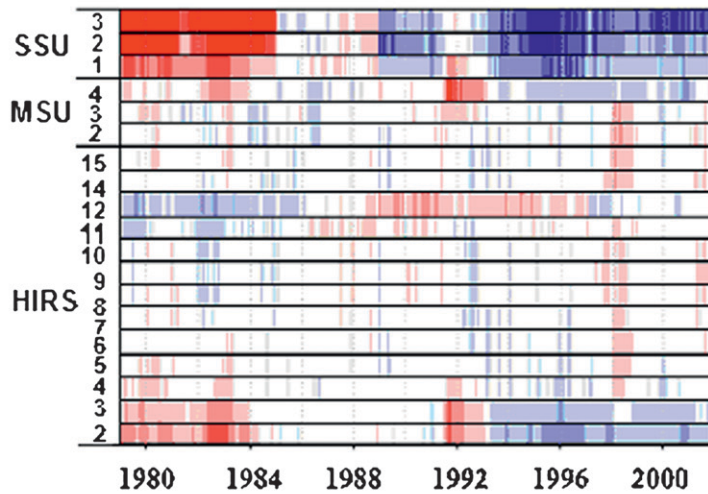From Eqs. (3) and (4), we obtain a relation between $\mathbf{D}_b$ and $\mathbf{b}_c$:

$$\mathbf{gavg}(\mathbf{b}_c) \cong \mathbf{gavg}(\mathbf{y}_o - \mathbf{y}_b) \cong (\mathbf{R} + \mathbf{H}\mathbf{B}\mathbf{H}^T)\mathbf{R}^{-1}\mathbf{D}_b$$

$$= (\mathbf{I} + \mathbf{H}\mathbf{B}\mathbf{H}^T\mathbf{R}^{-1})\mathbf{D}_b.$$

(5)

For an achievable calculation, it is usually assumed that the observational errors between channels do not have
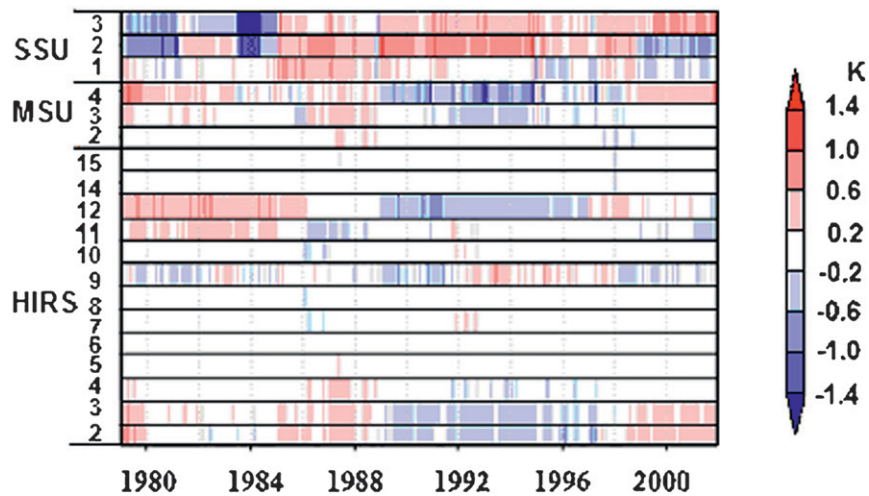
FIG. 7. Global average anomaly of estimated BT (K) using (a) JRA-25 and (b) ERA-40, and (c) their difference. Features of channels are shown in Table 3.

TABLE 3. TOVS channel features and usage in JRA-25 and ERA-40. The wavelengths/frequencies and peak energy contribution levels are after Werbowetzki (1981), and the usage in ERA-40 is after Hernandez et al. (2004).

Instrument	Channel No.	Central wavelength/ frequency	Peak energy contribution level (absorbing gas)	Usage in JRA-25	Usage in ERA-40
HIRS	2	14.71 μm	60 hPa (CO_2)	All condition	All condition
	3	14.49 μm	100 hPa (CO_2)	All condition	All condition
	4	14.22 μm	400 hPa (CO_2)	Clear ocean	Clear ocean
	5	13.97 μm	600 hPa (CO_2)	Clear ocean	Clear ocean
	6	13.64 μm	800 hPa (CO_2)	Clear ocean	Clear ocean
	7	13.35 μm	900 hPa (CO_2)	Clear ocean	Clear ocean
	10	8.16 μm	900 hPa (H_2O)	Clear ocean	
	11	7.33 μm	700 hPa (H_2O)	Clear ocean	Clear ocean
	12	6.72 μm	500 hPa (H_2O)	Clear ocean	Clear
	14	4.52 μm	950 hPa (CO_2, N_2O)		Clear ocean
	15	4.46 μm	700 hPa (CO_2, N_2O)	Clear ocean	Clear ocean
MSU	2	53.74 GHz	700 hPa (O_2)	Clear ocean	Ocean
	3	54.96 GHz	300 hPa (O_2)	Clear ocean	Ocean
	4	57.95 GHz	90 hPa (O_2)	All condition	All condition
SSU	1	15.0 μm	15.0 hPa (CO_2)	All condition	All condition
	2	15.0 μm	4.0 hPa (CO_2)	All condition	All condition
	3	15.0 μm	1.5 hPa (CO_2)	All condition	All condition

dependencies with each other. Therefore $\mathbf{R}$ and $\mathbf{R}^{-1}$ are diagonal. Since $\mathbf{HBH}^T$ is the error covariance matrix of $\mathbf{y}_b$, diagonal elements are rather dominant. Then Eq. (5) shows that $\mathbf{b}_c$ is nearly proportional to $\mathbf{D}_b$. Usually diagonal elements of $\mathbf{R}$ are larger than those of $\mathbf{HBH}^T$, therefore diagonal elements of $(\mathbf{I} + \mathbf{HBH}^T\mathbf{R}^{-1})$ are generally ranging from 1 to 2. In cases when the diagonal elements of $\mathbf{R}$ are several times larger than those of $\mathbf{HBH}^T$, as is traditionally shown in studies like Hollingsworth and Lönnberg (1986), $\mathbf{D}_b$ is nearly equal to $\mathbf{b}_c$. In the opposite cases when diagonal elements of $\mathbf{HBH}^T$ are relatively large, like ERA-40, and are comparable to those of $\mathbf{R}$, $\mathbf{b}_c$ approaches twice the magnitude of $\mathbf{D}_b$. Taking these into account, $\mathbf{b}_c$ and $\mathbf{D}_b$ are of the same order and $\mathbf{D}_b$ can be a good proxy of $\mathbf{b}_c$ as long as the calculation of 3DVAR is converged to an appropriate solution [the solution of 3DVAR is indirectly sought through an iterative calculation, because the actual dimension of $\mathbf{BH}^T(\mathbf{R} + \mathbf{HBH}^T)^{-1}$ is too large]. We show a schematic diagram of a simple example in Fig. 8, where there are four equally distanced observations of a single channel. In this case, $DB = \Sigma(BT_i - BT_i^*)$ and DB is equal to the bias to be corrected. Note that a positive DB indicates the reanalysis has a cooler BT* relative to BT.

The second metric is dependency (DP). This derives from a standard deviation of BT and a standard deviation of (BT − BT*) along the satellite track. We define monthly values of these; SDD is the standard deviation of (BT − BT*) and SDT is the standard deviation of raw BT. We then define the metric dependency of the reanalysis on the raw TOVS observation using the following formula:

$$DP = 100(\%) \times (SDT - SDD)/SDT. \quad (6)$$

From Eq. (2), we will see

$$\mathbf{y}_o - \mathbf{y}_a = \mathbf{y}_o - \mathbf{y}_b - (\mathbf{y}_a - \mathbf{y}_b) = (\mathbf{I} - \mathbf{HK})(\mathbf{y}_o - \mathbf{y}_b). \quad (7)$$

A vector of SDD for all channels $\mathbf{S}_{dd}$ is shown as $gstd(\mathbf{y}_o - \mathbf{y}_a)$, where gstd() is a global standard deviation:

$$\mathbf{S}_{dd} \cong [\mathbf{I} - \mathbf{HBH}^T(\mathbf{HBH}^T + \mathbf{R})^{-1}]\, gstd(\mathbf{y}_o - \mathbf{y}_b). \quad (8)$$

Here diagonal elements of $[\mathbf{I} - \mathbf{HBH}^T(\mathbf{HBH}^T + \mathbf{R})^{-1}]$ seem to be ranging from 0 to 1, and the equation shows that relatively large diagonal elements of $\mathbf{HBH}^T$ lead to small elements of $\mathbf{S}_{dd}$ and large DP. In the simple case of Fig. 8b, the variation of an analyzed value (BT*) accounts for a considerable part of the variation in the real observation (BT). DP compares the variation in TOVS BT (SDT) and the residual information after subtracting what BT* accounts for (SDD). If SDD is small relative to SDT, DP approaches 100%, which means that the reanalysis is highly dependent on TOVS BT.

Figure 9 presents the averages of monthly DB and DP over the period 1979–99. Because the two indices vary among spacecraft and time periods, they are presented as a kind of composite. The averaged DBs for both reanalyses seem similar for most of the channels. ERA-40 displays a better coherence with the raw TOVS observation for most of the channels as demonstrated by the higher DPs. Especially for SSU (an instrument for upper-stratospheric temperature sounding) and HIRS channels
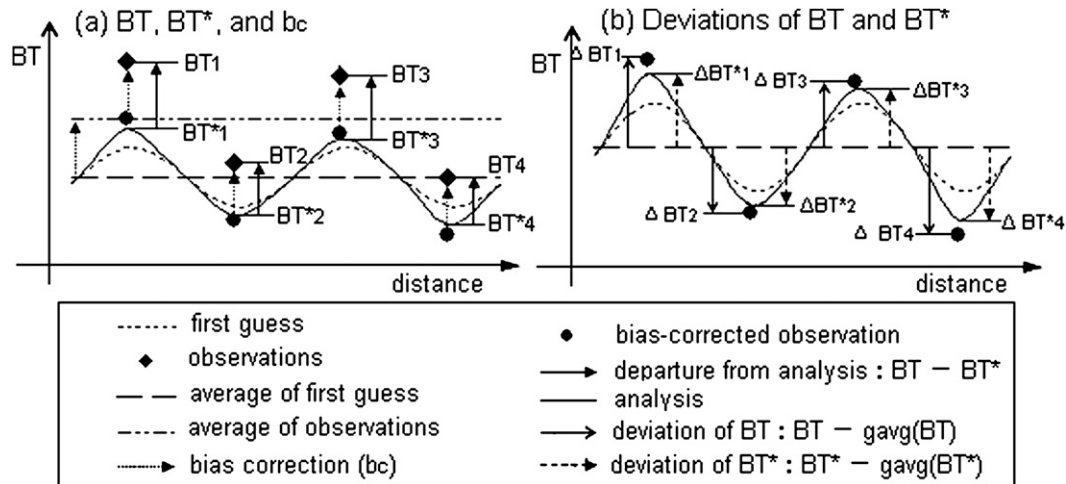
FIG. 8. Schematic diagrams of equally separated four observations in BT, a first guess field (a forecast), bias-corrected (b_c) observations, analysis field (reanalyses), and estimated values for observations (BT*) are shown. Directions of arrows indicate signs of each quantity; upward means plus, downward means minus. Since $DP = \Sigma(BT_i - BT_i^*)$ and in an ideal case the average of first guess is equal to that of the analysis, DP is equal to b_c. The variation of raw observations (the variation of BT_i) is equal to that of bias-corrected observations (i.e., the variation of ΔBT_i), and (b) the variation of ΔBT_i^* partly accounts for variation of that of ΔBT_i. The standard deviation of ΔBT_i is SDT, and that of $(\Delta BT_i - \Delta BT_i^*)$ is SDD. When a variation of ΔBT_i is perfectly coincident with that of ΔBT_i^*, SDD is zero and DP [Eq. (6)] is 100%. When observations are weakly assimilated or rejected, the analyzed field can be quite independent of the observations' variation. In the case when SDD becomes nearly comparable to SDT (if the forecast contains enough information), DP reaches 0%.

10–12 (tropospheric water vapor soundings), ERA-40 seems more closely tied to the TOVS observations than is JRA-25. This is consistent with the method in that ERA-40 used the larger forecast errors (**B**) in its DA system than in ECMWF's operational NWP. Also important is that Cardinali et al. (2004) suggest that the ECMWF DA system shows higher sensitivities to satellite radiances and somewhat lower sensitivities to raob systems.

b. The tropospheric temperature and moisture tendencies in the reanalyses

The reanalyses indicate different tendencies in BT* and different adjustments for HIRS channels 11 and 12 (Figs. 7 and 9 respectively). We begin with HIRS channel 11 (sensitive to water vapor around 700 hPa), which is reported to have the largest sensitivity in the ECMWF DA system (Cardinali et al. 2004). Figure 10 displays DB time series for each satellite, where ERA-40 shows more positive DB than JRA-25 in most periods.

The earlier spacecraft (TIROS-N to *NOAA-8*) seem to have particularly positive DBs (more than 1 K) for ERA-40. A positive DB means that the reanalysis has wetter conditions unless temperatures of the troposphere and/or surface are noticeably different. As Figs. 2 and 4 show, ERA-40 TLT and TMT in early years are generally similar to those of JRA-25, implying that ERA-40 has a wetter climate than JRA-25. However, a precise comparison of humidity distributions at 700 hPa reveals that ERA-40 is especially wetter than JRA-25 along the orbits of NOAA satellites while being drier elsewhere. Figure 11 shows 700-hPa specific humidity time series over an area (20°S–20°N, 150°E–date line) in the central western Pacific, differences [(ERA-40) − (JRA-25)] in specific humidity at 700 hPa, and each spot of HIRS channel 11 (BT* − BT) for ERA-40 in January 1980. For this period, TIROS-N and *NOAA-6* passed the area in the 0600 and 1800 UTC analysis time windows, but did not in the 0000 and 1200 UTC windows (although the TIROS-N passages became unstable in early 1980). As is shown in Figs. 11b,c, the raw HIRS channel 11 over the tropical ocean appears to be generally warmer than ERA-40 and the cool BT* of ERA-40 corresponds to the wetter difference relative to JRA-25. In Fig. 11a, ERA-40 shows an apparent 12-h cycle of fluctuations in specific humidity; when an operating satellite passes it becomes wetter in ERA-40, otherwise it is drier. This alternating feature seems strange, but it is consistent with the fact that ERA-40 has a particularly larger DP on this channel in comparison with JRA-25 (Fig. 9b).

Figure 10 shows other interesting features: (i) JRA-25 has larger DBs relative to ERA-40 only for the period from 1986 to 1988; (ii) JRA-25 DB decreases in the vicinity of the Mt. Pinatubo eruption in June 1991, while ERA-40 DB is unchanged.
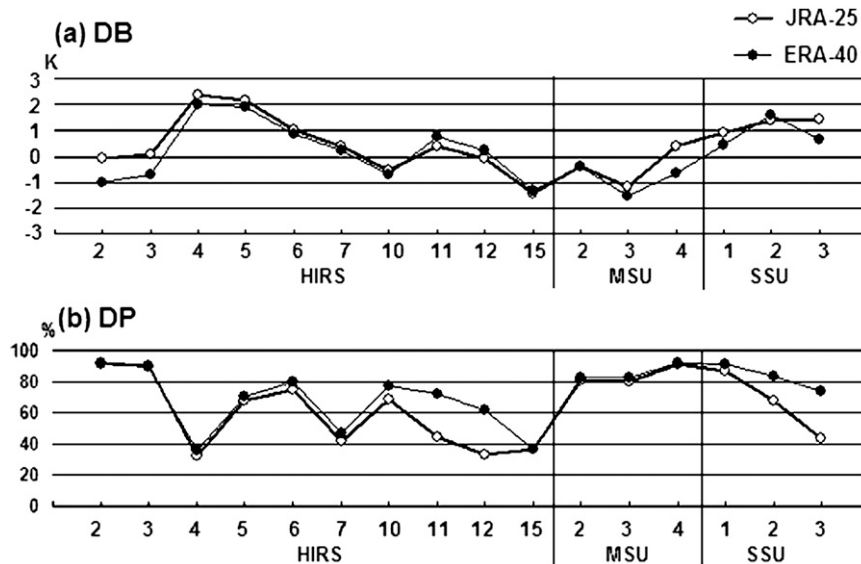
FIG. 9. DB (K) and DP (%) for JRA-25 (bold line) and ERA-40 (thin line). The averages over all spacecraft for the period from 1979 to 1999 are shown, taking erroneous observational periods into account.

Item (i) seems to derive from the different model responses to the 1986–87 ENSO event as was shown in Fig. 3a. However, around this incident, ERA-40 also experienced problems. This period follows ERA-40's sudden jump in HIRS channel 11 DB, which coincides with a sharp drop in its DP. The DP time sequences of HIRS channel 11 for *NOAA-9* are shown in Fig. 12. *NOAA-9* HIRS channel 11 observations might have been rejected in this period for some reason. *NOAA-9* did not have any co-orbiting NOAA satellite partner from February 1985 to November 1986, and there were no observations by the Special Sensor Microwave Imager (SSM/I) on the Defense Meteorological Satellite Program (DMPS) satellite yet. Therefore there were no dominant humidity observations over the ocean other than the *NOAA-9* HIRS. There may have been some problems in ERA-40's forecast model or boundary conditions around September 1985. Adding to these, there were two relays in the calculation streams in this period (Fig. 1).

Item (ii) appears to be related to the spurious water cycle drift in ERA-40 mentioned in Uppala et al. (2005), although they did not show objective evidence. We shall describe this episode by investigating HIRS channel 11 BT. The tropical (20°S–20°N) specific humidity anomaly at 700 hPa in Fig. 13a shows that ERA-40 has a positive shift by about 0.3g kg^{-1} in the vicinity of the Mt. Pinatubo eruption (June 1991). The additional moisture should be related to an increase in precipitation, and it actually increases by more than 0.5 mm day^{-1} in the tropical average as shown in Fig. 13b. Also

consistent with these is an enhancement of the upper-tropospheric (at 200 hPa) divergence out of the tropics by about 1.0×10^{-7} s^{-1} (not shown). Such an abrupt enhancement of the tropical hydrological cycle in ERA-40 corresponds with the HIRS channel 11 BT cooling. The difference in DB shown in Fig. 10 is about 0.5 K and ERA-40 DB is less than 1 K in this period. Considering Eq. (5) and the large forecast error in ERA-40, the actual bias correction used for this channel might be larger than DB. This may also partly account for the apparent warming seen in ERA-40 TLT trends over the subtropical ocean and the cooling inland of Africa (Fig. 3b), because the channel was used only over the ocean, and not over land (Table 3).

An enhancement in the atmospheric hydrologic cycle can cause significantly different vertical temperature and moisture structures. We show tropical (20°S–20°N) average temperature at 150 hPa and specific humidity at 300 hPa in Fig. 14. The upper-tropospheric temperature anomaly of ERA-40 is lower before 1991 and higher after 1991 relative to JRA-25, with only one exception during the period mentioned as item (i). For the periods 1986–90 and later 1991–96, ERA-40 depicts a drier climate in the upper troposphere (Fig. 14b). These upper-tropospheric temperature and moisture conditions correspond to a noticeable warming trend in ERA-40 BT* for HIRS channel 12 from the 1980s to 1990s (Fig. 7).

Given the evidence of these hydrologic and thermodynamic changes in ERA-40, it seems that the sudden enhancement in tropical water cycle in ERA-40 can
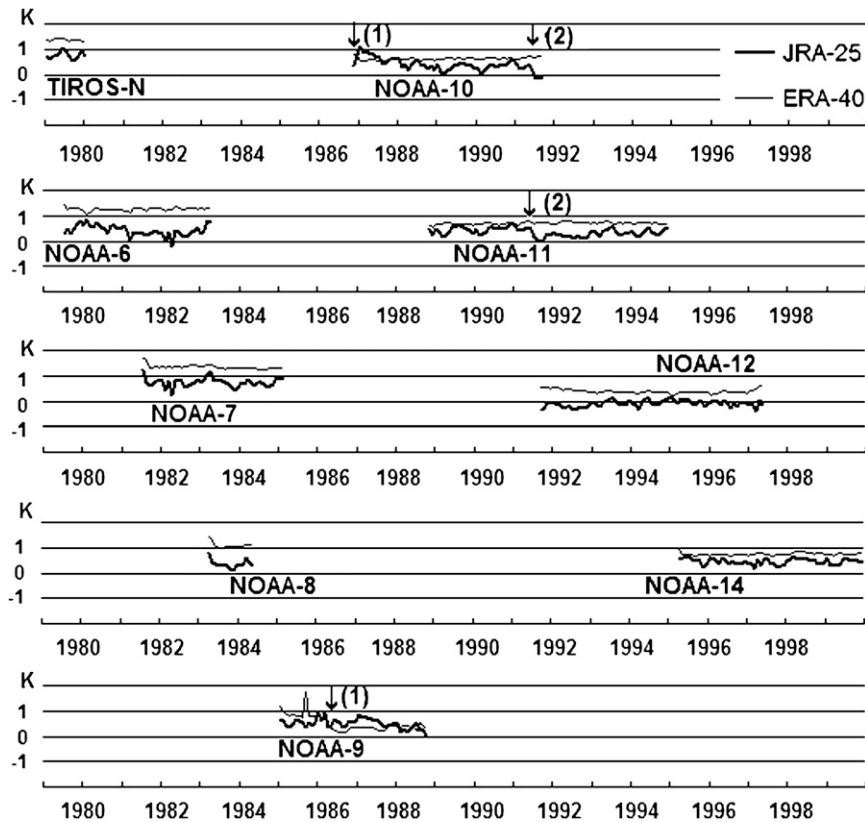
FIG. 10. DB (K) time series of HIRS channel 11 for JRA-25 (bold line) and ERA-40 (thin line). As for marks (1) and (2).

be explained by the problems in the bias correction for HIRS around the time of the Mt. Pinatubo eruption. Although the bias of 1 K seems small, this problem appears to extend through the water cycle. The vertical thermal structure in the tropics of ERA-40 appears to be seriously affected from then on, and the influence was extending to the subtropics. It is likely that ERA-40's upper-tropospheric temperature trend since 1979 is overly positive, which was related with the excessively positive TMT trend we noted earlier. This is consistent with Andersson et al. (2005) and Lanzante et al. (2006).

c. The lower-stratospheric temperature tendencies in the reanalyses

As shown in Figs. 6a and 6b, the globally averaged lower-stratospheric temperature is clearly influenced by the warming related to the volcanic aerosols of Mt. El Chichon (erupting in 1982) and Mt. Pinatubo (1991). There is also a noticeable variation in early 1989, when ERA-40, UAH, and RSS become warmer than JRA-25 (Figs. 6a and 6c). Since ERA-40 seems closer to UAH and RSS (Fig. 6d), this discrepancy seems to come from problems in JRA-25 and is worth discussing.

We examine DB and DP for MSU channel 4. DB time series are shown in Fig. 15. JRA-25 indicates unstable and positive DB, while ERA-40 has rather consistent and negative DB throughout the period except for TIROS-N.

ERA-40 DB for *NOAA-10* shifted in early 1989, and a sudden shift of ERA-40 DB is also found for *NOAA-9* in 1986. The shift in early 1989 seems to be associated with the advent of *NOAA-11*, but actually ERA-40 became warmer slightly later than November 1988 when *NOAA-11* appeared in both reanalyses. This was the point in time when ERA-40 started calculation stream 1 (Fig. 1). *NOAA-10* is considered to have a very stable MSU throughout its lifetime with only tiny drifts (order 0.01 K), so it can serve as a robust anchor for the period. However, ERA-40 seems to have applied different bias adjustments (by about 0.2 K) to *NOAA-10* midway into its operational period. Uppala et al. (2005) suggested that ERA-40 seems to have used different bias adjustments among the calculation streams. A shift found in 1986 is also coincident with the expiration of substream 5 (Fig. 1).

On the other hand, JRA-25 used unstable bias corrections even for *NOAA-10*'s MSU channel 4, because
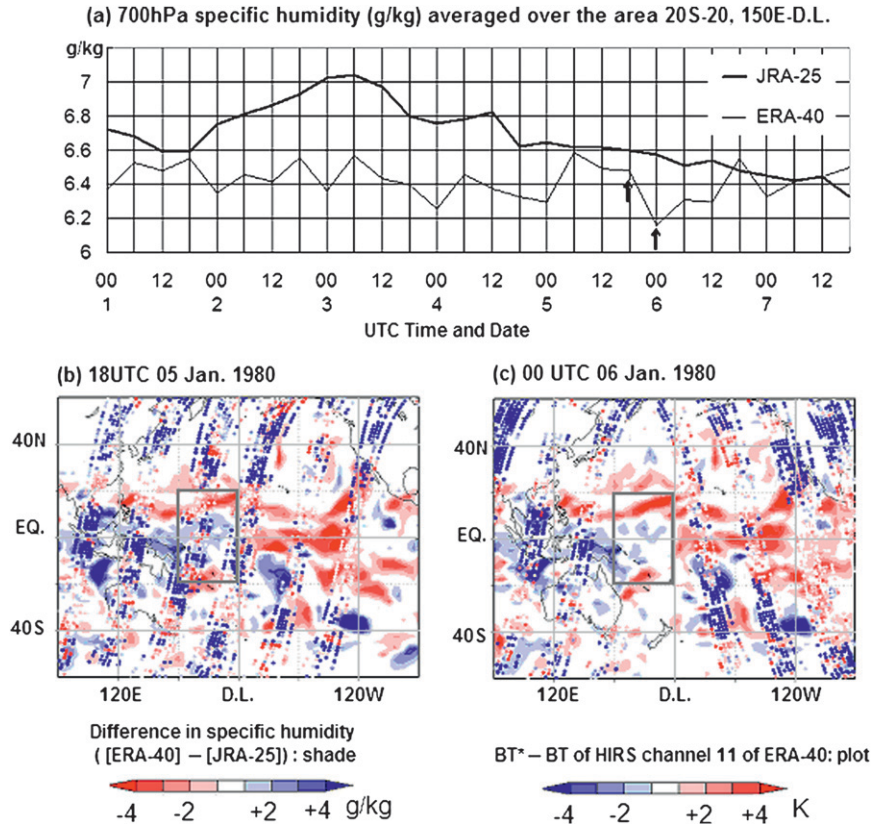
FIG. 11. (a) Specific humidity at 700 hPa averaged over (b),(c) area 20°S–20°N, 150°E–180° in the first 7 days in January 1980 (when TIROS-N and *NOAA-6* were available) for both re-analyses, and difference in specific humidity at 700 hPa [shade: (ERA-40) − (JRA-25 and BT* − BT of HIRS channel 11 for ERA-40 (plot) at (b) around 1800 UTC 5 Jan 1980 and (c) around 0000 UTC 6 Jan 1980. Specific humidity in g kg^{-1} (left legend) and BT* − BT in K (right legend) are shown in (b) and (c).

JRA-25 did not perform any offline intersatellite bias adjustments beforehand, and relied completely on its adaptive bias correction (appendix). Therefore JRA-25 did not have any effective anchor observations to which the long-term thermal behavior could be fixed. The GSM cooling bias (section 2a) was likely to have intensified this unstable nature. Because of the closer fit to the TLS products and its stable DB, ERA-40 seems more consistent than JRA-25. For *NOAA-10* and *-11*, ERA-40

has an especially large negative DB. Figures 6 and 15 suggest that *NOAA-10* and *-11* might have cool biases while TIROS-N likely has a warm bias, both of which affected JRA-25 considerably (Fig. 7).

There is another incident at this point that indicates inconsistencies in the reanalyses. We show the global anomaly of the total column ozone depth of the reanalyses in Fig. 16. ERA-40 ozone shows an apparent discontinuity in early 1989. Note that the ozone thickness
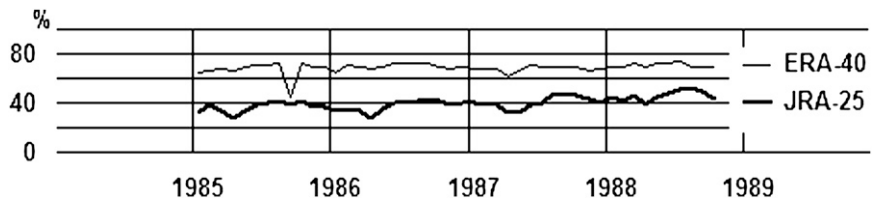

FIG. 12. DP (%) time series of HIRS channel 11 of *NOAA-9* for JRA-25 (bold line) and ERA-40 (thin line).
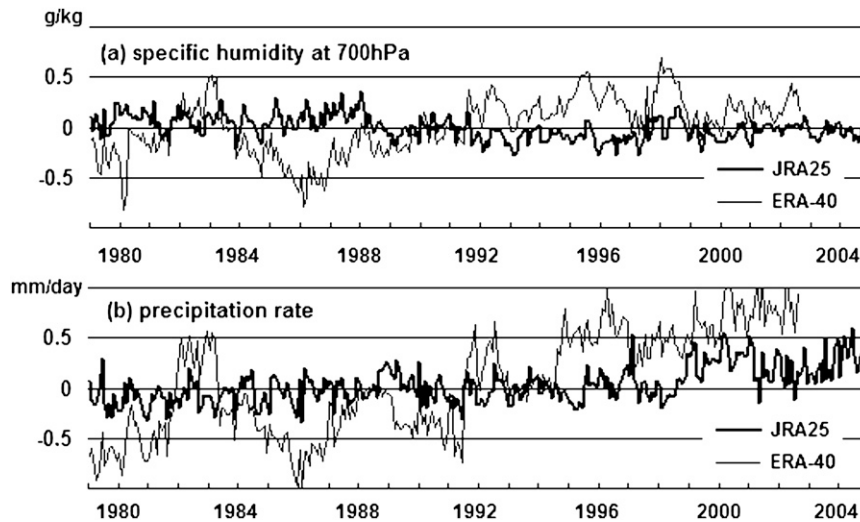
FIG. 13. Time sequences of (a) tropical (20°S–20°N) averaged anomaly specific humidity (g kg^{-1}) at 700 hPa and (b) tropical averaged precipitation rate anomaly (mm day^{-1}). The normal is calculated for the period 1979–2001.

shown here is the output of ERA-40 chemical transport estimation. Therefore, this is not the reason why the lower-stratospheric temperature changed.

JRA-25's time series of ozone concentrations shown here was used in the radiational heat flux calculations in GSM. The ozone data were prepared beforehand using the observations from TOMS of *Nimbus-7* and Earth Probe by NASA and meteorological profiles from ERA-40. A higher concentration of ozone around 1989 seems to have come from the higher temperatures of ERA-40. JRA-25's TLS cooling trend (Fig. 6a) shows

good agreement with the decreasing trend in Fig. 16. Such evidence indicates that lower-stratospheric temperature in JRA-25 seems to be closely tied to the radiative forcing related to the variation of ozone. For example, from May 1993 (when *Nimbus-7* TOMS expired) to July 1996 (when Earth Probe TOMS started), JRA-25 did not use much information from METOR-3 TOMS. Therefore, JRA-25 ozone appears unstable and with lower concentrations for this period. The colder and somewhat erratic temperature (Fig. 6a) corresponds well to this idea. This is also consistent with the
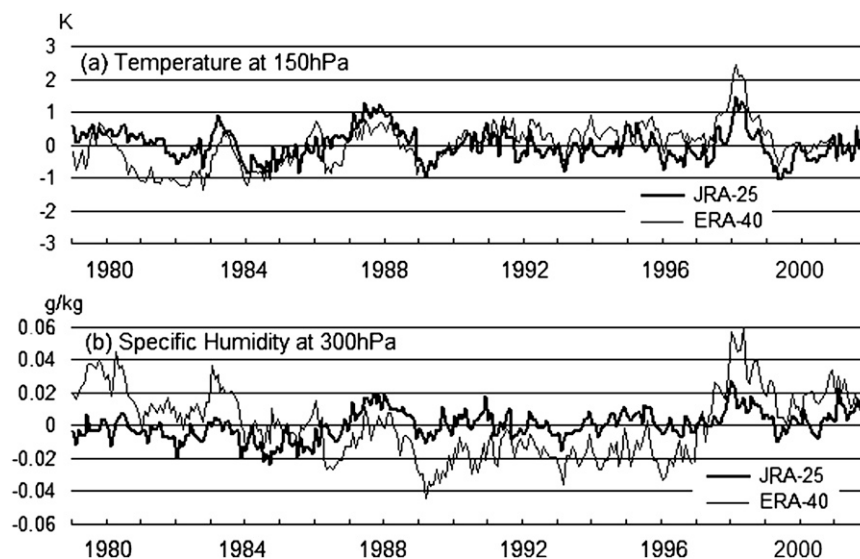

FIG. 14. (a) Tropical (20°S–20°N) averaged temperature anomaly (K) at 150 hPa, and (b) specific humidity (g kg^{-1}) at 300 hPa. The normal is calculated for the period 1979–2001.
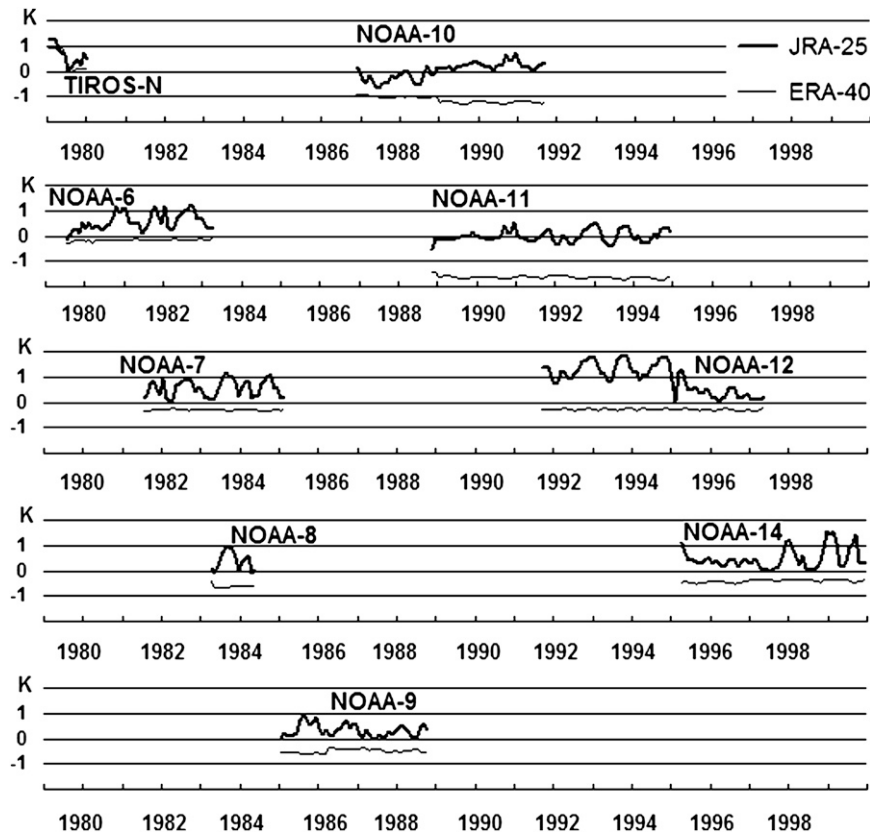
FIG. 15. DB (K) time series of MSU channel 4 for JRA-25 (bold line) and ERA-40 (thin line).

variations in the HIRS channel 9 BT estimation in Fig. 7a.

Although some documents (e.g., Onogi et al. 2007) blamed the TOVS usage in JRA-25 for this inconsistent behavior in the upper-air temperature, JRA-25 does not seem to be strongly constrained by the TOVS observations, at least in comparison with ERA-40, because it used the adaptive bias correction. JRA-25 unstable stratospheric temperature and the excessive cooling trend seem to derive chiefly from the inconsistencies in the GSM and the ozone data. The lower-stratospheric ozone concentration of JRA-25 is generally greater than ERA-40's (not shown). This also corresponds with the idea that the estimated BTs of HIRS channels 2 and 3 and MSU channel 4 in JRA-25 have relatively strong cooling trends in Fig. 7c. At the same time, ERA-40's cooling trend is apparent in the upper and middle stratosphere (SSU channels 2 and 3 in Fig. 7c).

5. Conclusions and implications

We have shown upper-air temperature tendencies of JRA-25 and ERA-40 in several comparisons with the observational bulk atmospheric layer products from

UAH and RSS. We then examined the usage of TOVS radiances in the reanalyses by comparing observed and simulated BTs. JRA-25 revealed the least positive TLT trend among the datasets and a negative TMT trend, while ERA-40 shows a significantly positive TMT trend. Our conclusion is that the trend of JRA-25 TLT is too negative and the trend of ERA-40 TMT is too positive. JRA-25 also displays considerably different TLS tendencies relative to the observations. These facts indicate that the precision of long-term thermal tendencies and trends in these second-generation reanalyses are still somewhat inconsistent with the observational datasets, so that further improvements are needed before climate trend and tendency studies may be confidently done.

JRA-25 used an adaptive bias correction in the TOVS system, which adjusted the biases using its background forecast. The GSM thermal bias in the lower stratosphere and the excessive decreasing trend of ozone have likely introduced errors into JRA-25's lower-stratospheric thermal tendencies. ERA-40 portrays a warmer tropical upper troposphere since the early 1990s relative to the 1980s, which is associated with the spurious sudden change in its hydrological cycle. In spite of the intensive
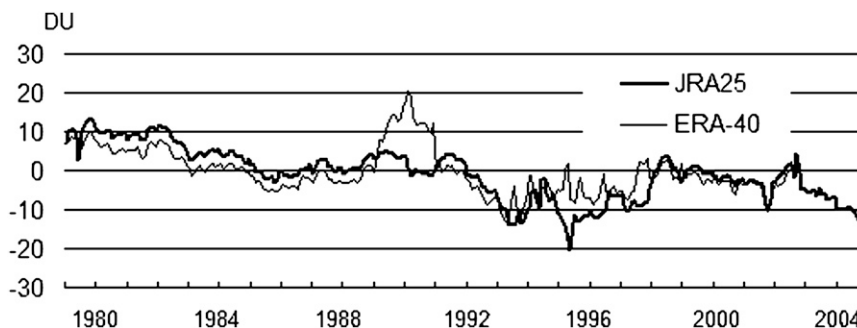
FIG. 16. Global average total column depth anomalies of ozone (DU) of JRA-25 and ERA-40. The normal is calculated for the period 1979–2001.

effort to improve the tropospheric water cycle features (Simmons et al. 1999), the upper-tropospheric temperature became warmer and the lower troposphere became wetter after the Mt. Pinatubo eruption. As reported by Andersson et al. (2005), this strong convection in the tropics and the strengthened Hadley circulation appear to be related to the TOVS assimilation. We see biases between HIRS channel 11 of observations and ERA-40 throughout the period of about 1 K, and this suggests the bias correction used in ERA-40 seems to be on the same order. It appears that the bias correction should be one of the most critical factors to improve, although Andersson et al. indicate the lack of TOVS assimilation in cloudy and rainy conditions as the most urgent challenge. We found that ERA-40 used inconsistent bias adjustments among its calculation streams, which introduced some sudden changes in climatic tendencies. This occurs because ERA-40 was constrained rather strictly by the TOVS observation as its large dependency score shows. Problems in both reanalyses seem to come from very different sources:

1) When the system (the forecast and DA system, and other observations besides TOVS) was not stable and reliable enough, an adaptive bias correction scheme like JRA-25 was not effective. Rather, a fixed bias correction value calculated from intersatellite comparisons beforehand should have been employed to correct the radiances.
2) With rather sophisticated systems and knowledge about TOVS intersatellite biases in their second reanalysis execution in ECMWF, an adaptive bias correction scheme, which already had been available, might have been more effective, especially to avoid the discontinuity at the volcanic eruption. When the forecast model was reliable, the larger forecast errors in the DA system do not seem to be necessarily effective. Relays of calculation streams inevitably bring unrealistic shifts between them.

Despite these problems, TOVS assimilation improves the analysis of the weather and climate features. We believe both reanalyses are useful in weather and climatic pattern detection, because they are based on the operational systems that are used for weather and climatic prediction. However, decade-to-decade comparisons and an estimation of the normal climate state are influenced by the problems described in this paper. Through the results of this study, we provide the following suggestions for future reanalysis teams.

1) A comprehensive observation dataset like the ERA-40 observing system will allow new organizations to attempt reanalysis construction. However, the system has gaps and drifts for certain platforms that lead to spurious shifts and trends if not accounted for. Preadjusting the TOVS radiances (and other quantities) before assimilation appears to be a viable option before attempting a reanalysis update.
2) Inconsistencies in the forecast model and DA systems also lead to inconsistencies in output reanalyses. Thus, using a single stream system with preadjusted forcing parameters such quantities as ozone, SST, and ice cover is important.

We anticipate better assimilation systems and better global models in the next generation of reanalyses that will achieve higher levels of consistency than we now see. For example, new bias correction schemes like the variational bias correction scheme (Dee 2005) will fill the small gaps at TOVS transitions. However, such adaptive bias corrections will reduce the climatic forcing effect of the TOVS observations. Even if time series appear to be smooth, this does not necessarily imply accurate climatic tendencies. We believe that the essential observations (TOVS, raob, etc.) should be independently adjusted to account for spurious shifts and drifts prior to use in data assimilation. Without the time-consuming work to attain the reliable observational

information (including the bias information), we will not be able to see a reasonable convergence to the observational evidence in future reanalyses.

To achieve these goals, it is important that multiple organizations continue their efforts to generate unique versions of analyses as mentioned in Karl et al. (2006). Each group is likely to discover important aspects of problems, which may be tested by other groups, leading to a higher level of confidence in the results. It is also clear in this study that more research at the reanalysis centers to understand their products more quantitatively is to be encouraged and expected in future. The authors also believe that academic communities should contribute to the improvement of any reanalysis, collaborating with reanalysis centers and rendering needed expertise.

APPENDIX

The Usage of TOVS in JRA-25

The quality control procedure for TOVS in JRA-25 is described here. As for the general features of the JRA-25 system, readers should refer to Onogi et al. (2007).

a. Cloud and rain detection

It is important to eliminate cloud and rain contamination prior to TOVS assimilation. JRA-25 used the following procedure for cloud and rain detection. Each spot of MSU was used after being combined with a single spot of HIRS, whose center is within 1.25° (in scan angle) from the MSU center. To examine the homogeneity of weather conditions in each MSU IFOV, HIRS channel 8 BT (BT_8) was examined,

$$|BT_8 - AVG_8| \leq STD_8,$$

where AVG_8 and STD_8 are an average and a standard deviation of BT_8 in each MSU IFOV, respectively. If there were not enough (eight or more) HIRS observations in each MSU IFOV, the spot was rejected because the homogeneity was unknown. This test examines if each MSU IFOV has rainy portions. The MSU

IFOV is more than 30 times as wide as HIRS, MSU is unable to detect small portions of rain accurately. According to McMillin and Dean (1982), window channels (8, 18, and 19) were used to determine the existence of clouds. Tests for daytime and nighttime are below.

A test for clear spots for daytime:

$$|BT_{18} - BT_8| \leq 10.0\,K.$$

Tests for clear spots for nighttime:

$$BT_{18} - BT_8 \leq 2.0\,K,$$
$$BT_8 - BT_{18} \leq 4.0\,K,$$
$$BT_{19} - BT_{18} \leq 2.0\,K,$$
$$BT_{18} - BT_{19} \leq 4.0\,K,$$

where BT_{18} and BT_{19} are observed BT of HIRS channels 18 and 19, respectively. To reject contamination by thin cirrus and/or thick aerosols, the difference between BT_8 and model skin surface temperature was tested. Assuming that the truly clear portion would range from 15% to 25% of the whole sky (Wylie and Menzel 1999), thresholds were adjusted in order to make sure that the clear rate would be kept within the range.

b. Channel selection

Channels that measure tropospheric emission and absorption were not used over land to avoid uncertain influences from land surface emissivities. The occupation ratio of land was examined for each HIRS and MSU, respectively. An IFOV that included more than 5% land portion was rejected. Near-infrared channels of HIRS except for channels 15, 18, and 19 were not used, because they seemed to be noisy in manual monitoring. HIRS channel 1 showed an unfavorable impact in assimilation experiments. JRA-25 channel selection is quite similar to that of ERA-40 (Table 3). Observations near limb scan positions seem very noisy when comparing with RTTOV version 6 estimation and thus were not used.

c. Bias correction

To obtain reasonable results in assimilation, eliminating the bias between observations and the first guess forecast [b_c in Eq. (4)] is very important. JRA-25 used the 1D-Var technique to estimate such biases. The residuals from the optimized profile were accumulated for bins of each BT range and for each scan position. The bias correction for each category bin was updated according to the following formula:

$$C_{n+1,i} = 15 \times C_{n,i}/16 + D_{n,i}/16,$$

where $C_{n,i}$ is the bias to be used for the ith channel in the nth DA cycle, and $D_{n,i}$ is an averaged residual in each category bin. An effective data number for each bin (EN) was tested, where

$$EN = \sum_{m=0}^{n-1} (N_{m,i} \times 15^{n-m-1}/16^{n-m}),$$

where $N_{m,i}$ is a sample number at the mth cycle. If EN was less than five, use of the channel in the category bin was suspended. To avoid overfitting to the first guess and excessive distortion from the original observation, when the bias correction ($C_{n,i}$) is larger than the observation error (o_e, a diagonal element of **R**), $C_{n,i}$ is substituted by $C'_{n,i}$:

$$C'_{n,i} = 2 \times o_e + 0.5 \times (C_{n,i} - 2 \times o_e).$$

d. Thinning and time window

As a sun-synchronous polar-orbiting satellite covers the whole globe during each 12 h, a 6-h time window leaves a considerable portion of the earth unobserved. Assimilation experiments prior to JRA-25 implied that partially covered dense TOVS observations, especially in the middle and upper stratosphere, affect unobserved regions. This is likely to be related to some limitation in 3DVAR, which assimilates all observations at the same time. The TOVS radiances were thinned to alleviate such problems and the assimilation time windows for the stratospheric channels were also extended up to 12 h. Observations outside of the normal 6-h window were thinned to be half-density of those inside the window.

REFERENCES

Andersson, E., and Coauthors, 2005: Assimilation and modeling of the atmospheric hydrological cycle in the ECMWF forecasting system. *Bull. Amer. Meteor. Soc.,* **86,** 387–402.

Andræ, U., N. Sokka, and K. Onogi, 2004: The radiosonde temperature bias corrections used in ERA-40. ECMWF ERA-40 Project Rep. Series 15, 34 pp.

Cardinali, C., S. Pezzulli, and E. Andersson, 2004: Influence-matrix diagnostic of a data assimilation system. *Quart. J. Roy. Meteor. Soc.,* **130,** 2767–2786.

Christy, J. R., and W. B. Norris, 2006: Satellite and VIZ–radiosonde intercomparisons for diagnosis of nonclimatic influences. *J. Atmos. Oceanic Technol.,* **23,** 1181–1194.

——, R. W. Spencer, and W. D. Braswell, 2000: MSU tropospheric temperatures: Dataset construction and radiosonde comparisons. *J. Atmos. Oceanic Technol.,* **17,** 1153–1170.

——, ——, W. B. Norris, W. D. Braswell, and D. E. Parker, 2003: Error estimates of version 5.0 of MSU–AMSU bulk atmospheric temperatures. *J. Atmos. Oceanic Technol.,* **20,** 613–629.

——, W. B. Norris, K. Redmond, and K. P. Gallo, 2006: Methodology and results of calculating central California surface

temperature trends: Evidence of human-induced climate change? *J. Climate,* **19,** 548–563.

——, ——, R. W. Spencer, and J. J. Hnilo, 2007: Tropospheric temperature change since 1979 from tropical radiosonde and satellite measurements. *J. Geophys. Res.,* **112,** D06102, doi:10.1029/2005JD006881.

Dee, D. P., 2005: Bias and data assimilation. *Quart. J. Roy. Meteor. Soc.,* **131,** 3323–3343.

Dethof, A., and E. Hólm, 2004: Ozone assimilation in the ERA-40 reanalysis project. *Quart. J. Roy. Meteor. Soc.,* **130,** 2851–2872.

Fiorino, M., 2002: Analysis and forecasts of tropical cyclones in the ECMWF 40-year reanalysis (ERA-40). Preprints, *25th Conf. on Hurricanes and Tropical Meteorology,* San Diego, CA, Amer. Meteor. Soc., 5D.2. [Available online at http://ams.confex.com/ams/pdfpapers/38743.pdf.]

Free, M., D. J. Seidel, J. K. Angell, J. Lanzante, I. Durre, and T. C. Peterson, 2005: Radiosonde Atmospheric Temperature Products for Assessing Climate (RATPAC): A new data set of large-area anomaly time series. *J. Geophys. Res.,* **110,** D22101, doi:10.1029/2005JD006169.

Fu, Q., C. M. Johanson, S. G. Warren, and D. J. Seidel, 2004: Contribution of stratospheric cooling to satellite-inferred tropospheric temperature trends. *Nature,* **429,** 55–58.

Gibson, J. K., P. Kållberg, S. Uppala, A. Hernandez, A. Nomura, and E. Serrano, 1997: ERA description. ECMWF ERA-15 Project Rep. Series 1, 72 pp.

Harris, B. A., and G. Kelly, 2001: A satellite radiance-bias correction scheme for data assimilation. *Quart. J. Roy. Meteor. Soc.,* **127,** 1453–1468.

Hernandez, A., G. Kelly, and S. Uppala, 2004: The TOVS/ATOVS observing system in ERA-40. ECMWF ERA-40 Project Rep. Series 16, 45 pp.

Hollingsworth, A., and P. Lönnberg, 1986: The statistical structure of short-range forecast errors as determined from radiosonde data. Part I: The wind field. *Tellus,* **38A,** 111–136.

Ishii, M., A. Shouji, S. Sugimoto, and T. Matsumoto, 2005: Objective analyses of sea-surface temperature and marine meteorological variables for the 20th century using ICOADS and the KOBE collection. *Int. J. Climatol.,* **25,** 865–879.

Jakob, C., and Coauthors, 2000: The IFS cycle CY21r4 made operational in October 1999. *ECMWF Newsletter,* No. 87, ECMWF, Reading, United Kingdom, 2–9.

JMA, 2002: Outline of the operational numerical weather prediction at the Japan Meteorological Agency. Appendix to WMO Numerical Weather Prediction Progress Rep., Japan Meteorological Agency, 158 pp.

Kalnay, E., and Coauthors, 1996: The NCEP/NCAR 40-Year Reanalysis Project. *Bull. Amer. Meteor. Soc.,* **77,** 437–471.

Karl, T. R., S. J. Hassol, C. D. Miller, and W. L. Murray, 2006: *Temperature Trends of the Lower Atmosphere: Steps for Understanding and Reconciling Differences.* Synthesis and Assessment Product 1.1, Climate Change Science Program and the Subcommittee on Global Change Research Rep., 180 pp.

Lanzante, J. R., T. C. Peterson, F. J. Wentz, and K. Y. Vinnikov, 2006: What do observations of temperatures in the atmosphere and at the surface since the advent of measuring temperatures vertically? *Temperature Trends of the Lower Atmosphere: Steps for Understanding and Reconciling Differences.* T. R. Karl et al., Eds., Synthesis and Assessment Product 1.1, Climate Change Science Program and the Subcommittee on Global Change Research Rep., 47–70.

McMillin, L. M., and C. Dean, 1982: Evaluation of a new operational technique for producing clear radiances. *J. Appl. Meteor.,* **21,** 1005–1014.

Mears, C. A., and F. J. Wentz, 2005: The effect of diurnal correction on satellite-derived lower tropospheric temperature. *Science,* **309,** 1548–1551.

——, M. C. Schabel, and F. J. Wentz, 2003: A reanalysis of the MSU channel 2 tropospheric temperature record. *J. Climate,* **16,** 3650–3664.

Murai, S., S. Yabu, and H. Kitagawa, 2005: Development of a new radiation scheme for the global atmospheric NWP model. Preprints, *21st Conf. on Weather Analysis and Forecasting/17th Conf. on Numerical Weather Prediction,* Washington, DC, Amer. Meteor. Soc., P1.66. [Available online at http://ams.confex.com/ams/pdfpapers/94316.pdf.]

Onogi, K., and Coauthors, 2005: JRA-25: Japanese 25-year reanalysis project—Progress and status. *Quart. J. Roy. Meteor. Soc.,* **131,** 3259–3268.

——, and Coauthors, 2007: The JRA-25 reanalysis. *J. Meteor. Soc. Japan,* **85,** 369–432.

Oyama, R., 2007: Characteristics and effectiveness of Atmospheric Motion Vector product (AMV) in Japanese long-term Reanalysis project (JRA-25) (in Japanese). Meteorological Satellite Center Tech. Note 48, 1–36.

Randall, R. M., and B. M. Herman, 2008: Using limited time period trends as a means to determine attribution of discrepancies in microwave sounding unit-derived tropospheric temperature time series. *J. Geophys. Res.,* **113,** D05105, doi:10.1029/2007JD008864.

Reynolds, R. W., N. A. Rayner, T. M. Smith, and D. C. Stokes, 2002: An improved in situ and satellite SST analysis for climate. *J. Climate,* **15,** 1609–1625.

Santer, B. D., and Coauthors, 2004: Identification of anthropogenic climate change using a second-generation reanalysis. *J. Geophys. Res.,* **109,** D21104, doi:10.1029/2004JD005075.

Saunders, R., M. Matricardi, and P. Brunel, 1999: An improved fast radiative transfer model for assimilation of satellite radiance observations. *Quart. J. Roy. Meteor. Soc.,* **125,** 1407–1425.

Simmons, A. J., A. Untch, C. Jakob, P. Kållberg, and P. Undén, 1999: Stratospheric water vapour and tropical tropopause temperatures in ECMWF analyses and multi-year simulations. *Quart. J. Roy. Meteor. Soc.,* **125,** 353–386.

Smith, W. L., H. M. Woolf, C. M. Hayden, D. Q. Wark, and L. M. McMillin, 1979: The TIROS-N operational vertical sounder. *Bull. Amer. Meteor. Soc.,* **60,** 1177–1187.

Spencer, R. W., and J. R. Christy, 1990: Precise monitoring of global temperature trends from satellites. *Science,* **247,** 1558–1562.

——, and ——, 1992a: Precision and radiosonde validation of satellite gridpoint temperature anomalies. Part I: MSU channel 2. *J. Climate,* **5,** 847–857.

——, and ——, 1992b: Precision and radiosonde validation of satellite gridpoint temperature anomalies. Part II: A tropospheric retrieval and trends during 1979–1990. *J. Climate,* **5,** 858–866.

Takeuchi, Y., and T. Tsuyuki, 2002: The operational 3DVAR assimilation system of JMA for the global spectra model and the typhoon model. CAS/JSC WGNE Research Activities in Atmospheric and Oceanic Modeling, WMO/TD-1105, No. 32, 1.59–1.60.

Thorne, P. W., D. E. Parker, S. F. B. Tett, P. D. Jones, M. McCarthy, H. Coleman, and P. Brohan, 2005: Revisiting radiosonde upper air temperatures from 1958 to 2002. *J. Geophys. Res.,* **110,** D18105, doi:10.1029/2004JD005753.

Uppala, S. M., and Coauthors, 2005: The ERA-40 Re-Analysis. *Quart. J. Roy. Meteor. Soc.,* **131,** 2961–3012.

Werbowetzki, A., 1981: Atmospheric sounding user's guide. NOAA Tech. Rep. NESS 83, 82 pp.

Wylie, D. P., and W. P. Menzel, 1999: Eight years of high cloud statistics using HIRS. *J. Climate,* **12,** 170–184.